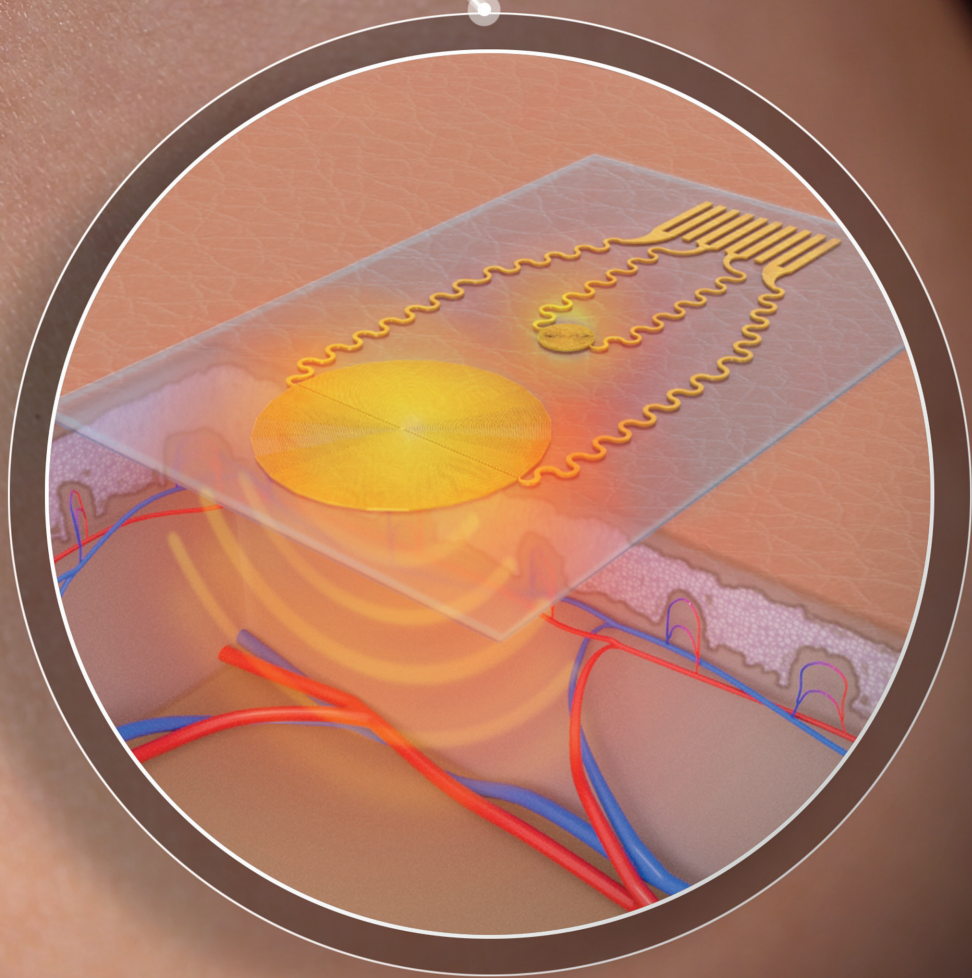
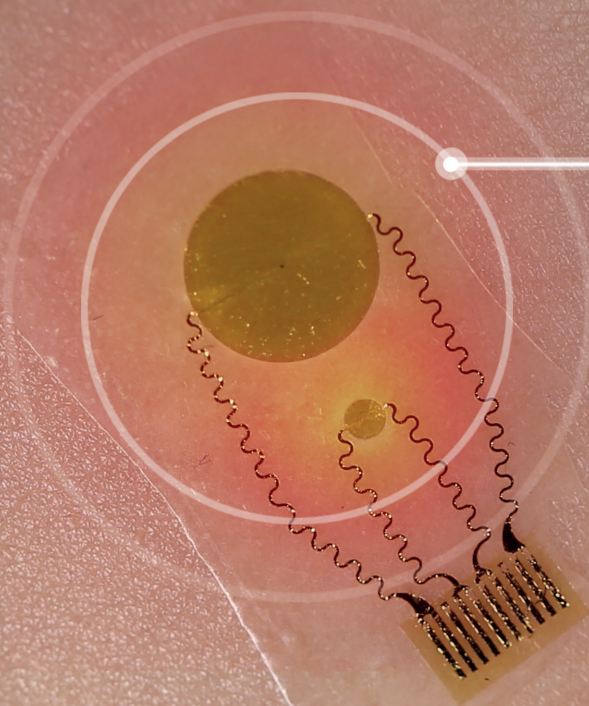


ADVANCED FUNCTIONAL MATERIALS



Epidermal Electronic Systems for Measuring the Thermal Properties of Human Skin at Depths of up to Several Millimeters

Surabhi R. Madhvapathy, Yinji Ma, Manish Patel, Siddharth Krishnan, Chen Wei, Yajing Li, Shuai Xu, Xue Feng, Yonggang Huang,* and John A. Rogers*

Monitoring the composition, blood flow properties, and hydration status of human skin can be important in diagnosing disease and tracking overall health. Current methods are largely limited to clinical environments, and they primarily measure properties of superficial layers of the skin, such as the stratum corneum (10–40 μm). This work introduces soft, skin-like thermal depth sensors (e-TDS) in designs that seamlessly couple with human skin and measure its thermal properties with depth sensitivity that can extend up to 6 mm beneath the surface. Guidelines for tailoring devices to enable measurements through different effective depths follow from a systematic set of experiments, supported by theoretical modeling. On-body testing validates the physiological relevance of measurements using the e-TDS platform, with potential to aid the diagnosis of deep cutaneous and systemic diseases. Specific demonstrations include measurements that capture responses ranging from superficial changes in skin properties that result from application of a moisturizer, to changes in microvascular flow at intermediate depths induced by heating/cooling, to detection of inflammation in the deep dermis and subcutaneous fat in an incidence of a local bacterial infection, cellulitis.

1. Introduction

Biophysical/chemical measurements performed through the skin represent attractive modalities for the noninvasive assessment of a wide range of bodily structures and functions.^[1] Deriving insights into physiological processes that extend beyond the uppermost layers of the epidermis ($\approx 100 \mu\text{m}$ thickness) by capturing parameters related to deep tissue inflammation, core body temperature, or core body hydration remain as key challenges.^[2] Quantitative techniques such as corneometry and laser Doppler flowmetry can apply only to immobilized patients and they require specialized, expensive equipment. Methods such as ultrasound, computer-aided tomography (CT), and magnetic resonance imaging (MRI) require long measurement times, clinical expertise for

S. R. Madhvapathy, M. Patel, Dr. Y. Li
Department of Materials Science and Engineering
Center for Bio-Integrated Electronics
Simpson Querrey Institute for Nano/Biotechnology
Northwestern University
Evanston, IL 60208, USA

Prof. Y. Ma, Prof. X. Feng
AML Department of Engineering Mechanics
Interdisciplinary Research Center for Flexible Electronics Technology
Tsinghua University
Beijing 100084, P. R. China

S. Krishnan
Department of Materials Science and Engineering
Frederick Seitz Materials Research Laboratory
University of Illinois at Urbana-Champaign
Urbana, IL 61801, USA

S. Krishnan
Center for Bio-Integrated Electronics
Northwestern University
Evanston, IL 60208, USA

C. Wei
Department of Mechanical Engineering
Northwestern University
Evanston, IL 60208, USA

Dr. S. Xu
Department of Dermatology
Feinberg School of Medicine
Center for Bio-Integrated Electronics
Simpson Querrey Institute for Nano/Biotechnology
Northwestern University
Chicago, IL 60611, USA

Prof. Y. Huang
Departments of Civil and Environmental Engineering
and Mechanical Engineering
Center for Engineering Health, and Skin Disease Research Center
Northwestern University
Evanston, IL 60208, USA
E-mail: y-huang@northwestern.edu

Prof. J. A. Rogers
Departments of Materials Science and Engineering, Biomedical
Engineering, Chemistry, Mechanical Engineering, Electrical
Engineering and Computer Science, and Neurological Surgery
Center for Bio-Integrated Electronics
Simpson Querrey Institute for Nano/Biotechnology
McCormick School of Engineering and Feinberg School of Medicine
Northwestern University
Evanston, IL 60208, USA
E-mail: jrogers@northwestern.edu

 The ORCID identification number(s) for the author(s) of this article can be found under <https://doi.org/10.1002/adfm.201802083>.

DOI: 10.1002/adfm.201802083

interpretation, high cost, and they can involve risks associated with irradiation.^[3] Clinical visual inspection often leads to high misdiagnosis rates for pathologies that appear similar at the surface of the skin.^[4] Thus, there is a continued need for inexpensive and robust point-of-care sensors capable of capturing broader insights into human physiology and disease.

Measurements of the thermal properties of the skin with thin, skin-interfaced device platforms are attractive because they can be accomplished in a noninvasive manner, without significant motion artifacts or direct input of electrical current into the skin.^[5] Thermal conductivity (k) and thermal diffusivity (α) are useful parameters as they lend insight into a wide range of physiological characteristics including tissue composition, local blood flow, and tissue hydration.^[6] The transient plane source (TPS) technique can capture these properties in a real-time fashion, with capabilities in depth profiling which follow from the governing physics of thermal diffusion and conduction.^[7] Advanced device embodiments in thin, elastomeric forms facilitate such measurements on human skin, yet prior studies focus only on measurements of superficial layers ($\approx 5\ \mu\text{m}$ to $1\ \text{mm}$), thereby limiting applications to the skin surface.^[5b,6,8]

In this work, we present soft, skin-like sensors that evaluate k at different depths of skin and tissue up to $6\ \text{mm}$ beneath the surface. The epidermal sensors presented here are conformal to the skin, soft, stretchable, reusable, and noninvasive. The good adhesion and conformity of the device to the skin assist in efficient heat transfer between the sensor and the skin. Studies of heat transport reveal optimized measurement conditions and sensor designs for controlled levels of depth sensitivity. Specifically, experimental and theoretical investigations on well-defined material structures that mimic the skin establish key parameters that provide the framework for a tunable depth-sensing system. Use of these sensors in various investigations with human subjects yields insights into physiological changes in the skin via thermal property measurements. The results, which represent the first demonstrations of a noninvasive, skin-interfaced sensor with capabilities for large measurement depths, have the potential to uncover important physiological and clinical parameters in ways that bypass limitations of other approaches.

2. Results and Discussion

2.1. Device Structure and Operation Using a Single-Layer Model

Each epidermal thermal depth sensor (e-TDS) consists of a thin metal trace (Au, $5\text{--}10\ \mu\text{m}$ width) in a circular, coil geometry (radius R), with a pair of serpentine interconnects (Au, $100\ \mu\text{m}$ width and length $\approx 2R$, with resistance $< 100\ \Omega$) and corresponding bond pads for external wiring (Figure 1a,b). Layers of polyimide (PI) on top and bottom electrically insulate these traces. A thin layer of silicone elastomer serves as a substrate that allows repeated cycles of conformal contact and release from surfaces of samples under test. The detailed fabrication process is discussed in the “Experimental Section.”

To understand the physics of heat transport associated with these devices, consider measurements on a homogeneous, semi-infinite substrate (silicone, whose thermal properties are in the range of those of human skin) doped with a thermochromic

dye that changes its color from black to pink at $T \approx 25\ ^\circ\text{C}$. Injecting direct current (DC) electrical power into the sensing coil, with power per unit area of q , at some initial time, creates an increase in temperature throughout a localized area of material. The corresponding changes in color occur with spatiotemporal characteristics that reflect the thermal physics (Figure 1c–e). Specifically, the heat spreads with time, downward into the substrate and radially in the plane by similar distances due to the isotropic nature of heat conduction in this material system (see Video S1 in the Supporting Information). Wiring and data acquisition are described in the “Experimental Section” and Figure S1 (Supporting Information). Finite element analysis (FEA) (Figure 1f–h) quantitatively captures the observed behaviors and their dependence on the thermal conductivity and diffusivity (k and α) of the material and the value of q . The temperature of the sensing coil (T) increases from its initial value by an amount ΔT that depends on time (t) after initiation of thermal actuation. ΔT depends linearly on q for all materials and heating conditions investigated in this work (Figure S1, Supporting Information). As a result, linear thermal analysis by FEA can be used to extract k from the measured ΔT , given known values of α , R , t , and q (details on TPS measurements and FEA fitting are in the “Experimental Section”). All FEA simulations consider the thermal properties of each layer of the e-TDS, including the PI encapsulation and elastomer substrate.

Unlike silicone and other standard materials, human skin can display large variations in thermal properties, and thus the values α and k are generally unknown.^[6d,9] This work considers k as the most relevant thermal parameter to characterize human skin because it is linearly related to physiological properties such as skin water content and, by comparison to α , it can be extracted with higher accuracy using fits to FEA.^[6c] During the initial rise in temperature after thermal actuation, both α and k affect the thermal response; at longer times, when ΔT reaches a quasi-steady-state value, only k is important. For practical applications outlined here, the e-TDS operates in this latter regime (when $t > t_{\text{min}}$, typically a few tens of seconds for skin). In addition to FEA, an analytical scaling law that relates α to ΔT reveals that knowledge of α is not necessary for accurate extraction of k from ΔT measured for $t > t_{\text{min}}$ (Figure S2 and Table S1, Supporting Information). Specifically, calculations show that in this quasi-steady-state regime, ΔT varies by $< 5\%$ for values of α across the full physiological range. The following studies focus on measurements in this regime.

2.2. Depth Sensitivity of e-TDS Using a Multilayer Model for Human Skin

Human skin is inhomogeneous and comprises three layers. The outermost layer is the epidermis and acts as a water-proof barrier. Beneath it, the dermis consists of collagen and imparts the mechanical strength of skin. Finally, deeper subcutaneous tissue contains fat and additional connective tissue. Each layer exhibits different α and k due to variations in composition, blood flow, and water content.^[5b,6a,d] All of these layers affect, to different degrees, the ΔT measured by an e-TDS. Studies reported here approximate the skin as a bilayer system to simplify analysis and allow assessment

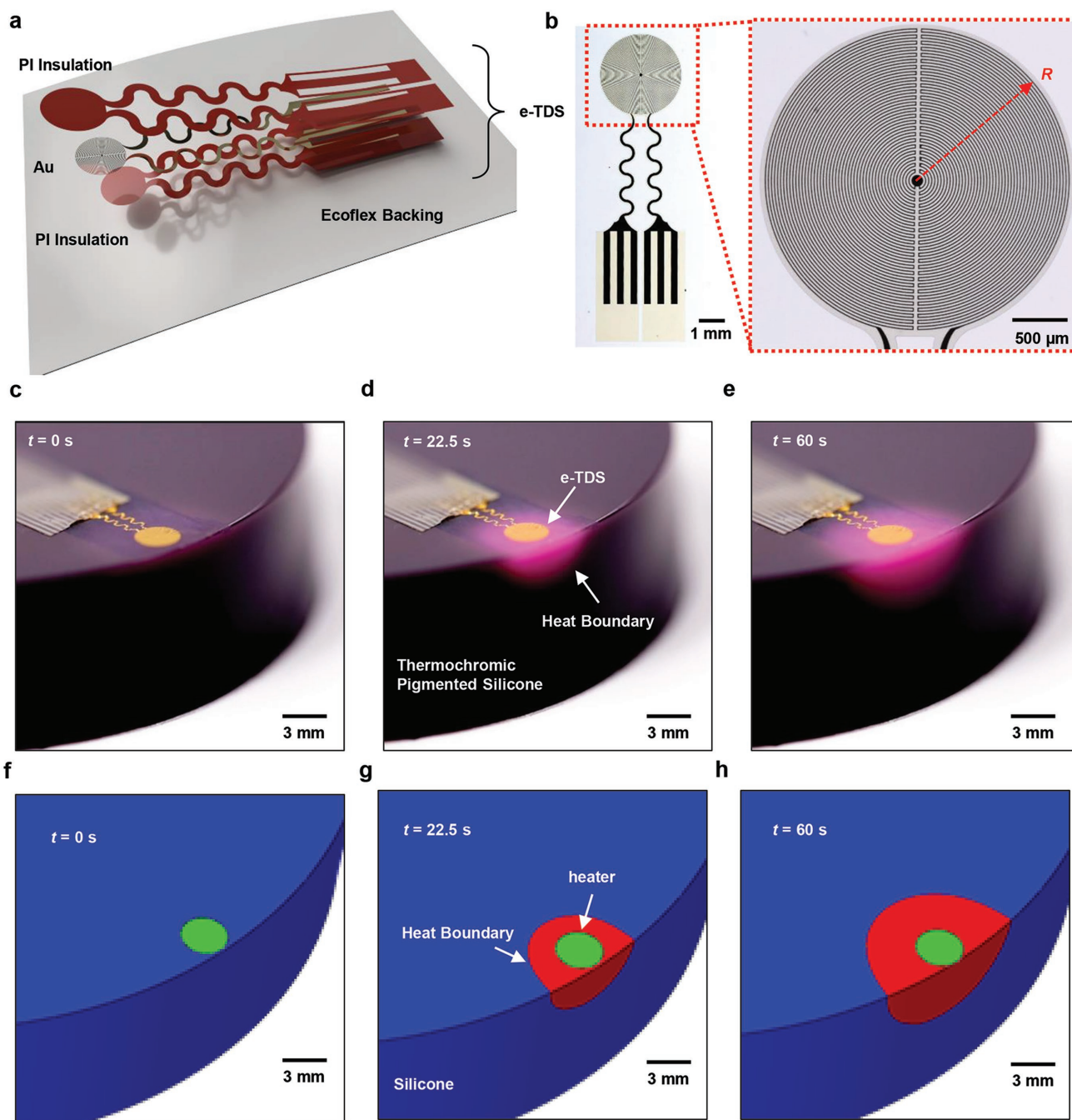


Figure 1. Principle of operation of epidermal thermal depth sensors (e-TDS). a) Illustration of the layers of a representative e-TDS. b) Optical image and magnified view of an e-TDS with a coil of radius R . c) Image of an e-TDS printed onto silicone (Ecoflex) mixed with a thermochromic pigment that turns from black to pink for temperatures above 25 °C. Image is taken at ambient temperature $T = 22$ °C, before the heater is turned ON ($t = 0$ s). Image of the same sensor as in panel (b) for an applied power density of $q = 10$ mW mm⁻² at d) $t = 22.5$ s and e) $t = 60$ s. f) Cross-sectional view of FEA results for an e-TDS with $R = 1.5$ mm, and an applied power density of $q = 10$ mW mm⁻² at t = 0 s, g) $t = 22.5$ s, and h) $t = 60$ s. The red shaded region indicates the area of silicone that is at $T \geq 25$ °C.

of the choice of e-TDS designs and measurement conditions on ΔT , all in the context of extracting accurate values of k . In this treatment, the epidermis and dermis (E+D) form the top layer (the epidermis is $0.1 \times$ as thick as the dermis)^[10] and the subcutaneous fat constitutes the bottom layer. A test bilayer sample of tailored formulations of poly(dimethylsiloxane)

(PDMS) can approximate the thermal properties of human skin and fat (Figure 2a). In particular, silicone A (Sylgard 170 (S170), Dow-Corning, $k_A = 0.47$ W m⁻¹ K⁻¹ and $\alpha_A = 0.14$ mm² s⁻¹)^[11] has thermal properties similar to those of human skin (E+D, $k = 0.25$ – 0.45 W m⁻¹ K⁻¹)^[6,9,12], and silicone B (Sylgard 184 (S184), Dow-Corning, $k_B = 0.21$ W m⁻¹ K⁻¹

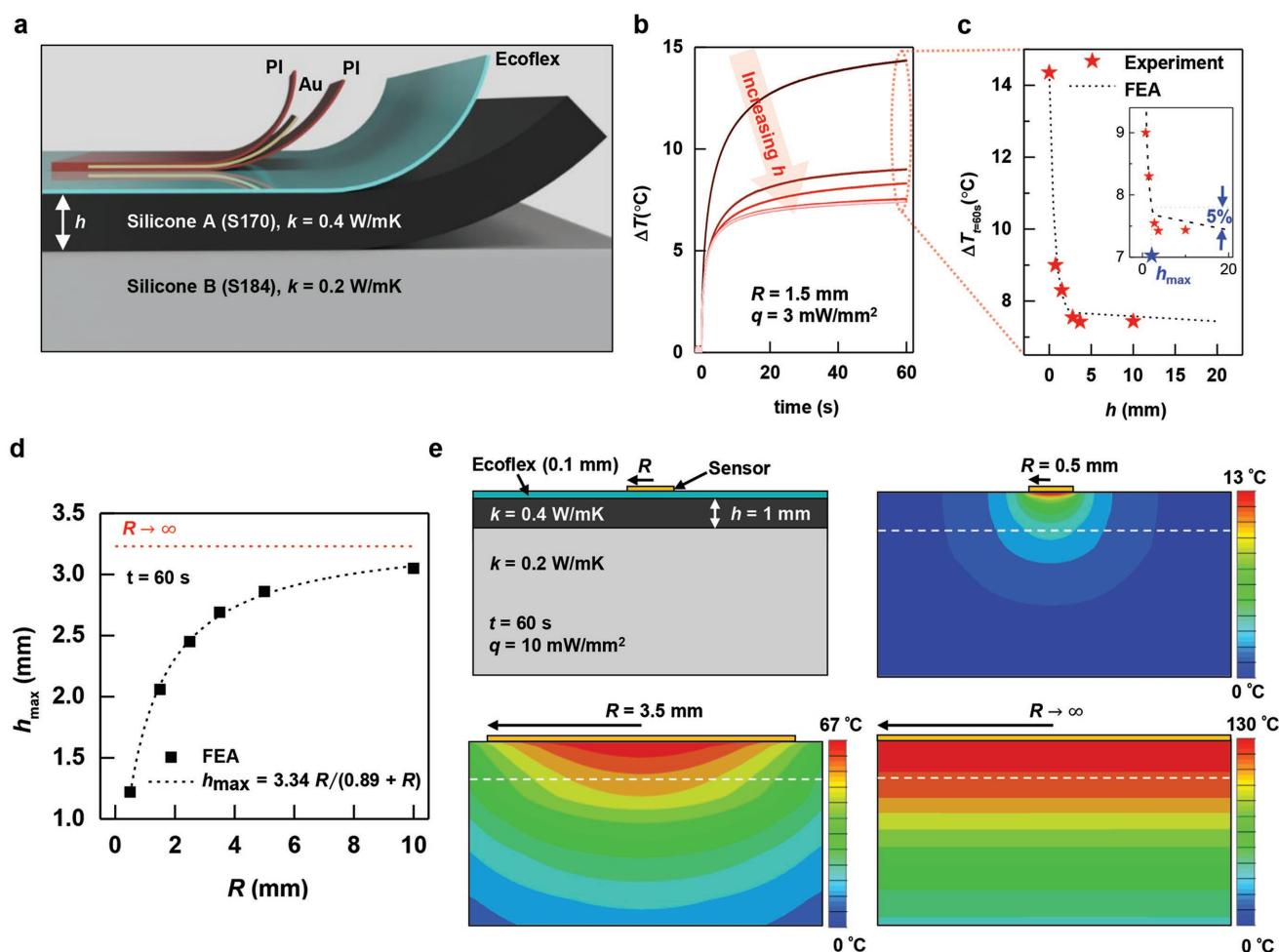


Figure 2. Dependence of depth sensitivity (h_{\max}) on radius of the e-TDS. a) Schematic illustration of an e-TDS mounted on a bilayer silicone sample designed to characterize the depth sensitivity of the measurement. b) Change in temperature (ΔT) as a function of time for an e-TDS with $R = 1.5$ mm and $q = 3$ mW mm $^{-2}$. The thickness of the silicone A layer (h) increases in the direction indicated by the arrow. c) ΔT at $t = 60$ s as a function of h . The procedure to calculate the 5% threshold for depth sensitivity (h_{\max}) is described in the inset of the panel (c). d) h_{\max} as a function of R determined from FEA simulations. The red dotted line represents the limiting value of h_{\max} for an infinitely large e-TDS at a measurement time of 60 s. The dotted line represents an analytical fit of the FEA calculations with adjusted R -squared = 0.998. e) Cross-sectional schematic image showing the parameters used for the FEA simulations, and the corresponding temperature contour maps for $t = 60$ s measurement time and $q = 10$ mW mm $^{-2}$, for varying R .

and $\alpha_B = 0.11$ mm 2 s $^{-1}$ ^[6b]) has thermal properties comparable to subcutaneous fat ($k = 0.18$ – 0.23 W m $^{-1}$ K $^{-1}$ ^[9,12]).

The maximum depth below the surface (h_{\max}) up to which that the e-TDS can sense thermal properties depends on the sensor design (R) and measurement conditions (t) for a fixed bilayer system (k_A , k_B , α_A , and α_B) (as discussed in the “Experimental Section” on FEA modeling, h_{\max} also depends on the nature of heat transport into the air). Measurements with a given e-TDS ($R = 1.5$ mm and $q = 3$ mW mm $^{-2}$) on silicone bilayer samples with various thicknesses of silicone A (h) reveal the functional dependence of the response on h_{\max} (Figure 2b). The ΔT versus t curves captured from such samples overlap with measurements on a semi-infinite substrate of silicone A (ΔT_A) when $h > h_{\max}$. We consider ΔT at $t = 60$ s $>$ t_{\min} (and hence the quasi-steady-state regime) for all values of h , extracted from the sensors’ ΔT versus h output (Figure 2c), for the purpose of analyzing k . The largest value of h for which

ΔT is larger than ΔT_A by 5% (Equation (1)) defines h_{\max} . In particular,

$$\frac{\Delta T(h = h_{\max}) - \Delta T_A}{\Delta T_A} = 5\% \quad (1)$$

The 5% threshold corresponds to the maximum relative standard error (RSE) in measurements of ΔT_A . Three-fold measurements of ΔT_A for every e-TDS of radius R yield the RSE, as given by

$$\text{RSE} = \frac{(1/\sqrt{3})\sigma_{\Delta T_A}}{\Delta T_A} \quad (2)$$

where $\sigma_{\Delta T_A}$ is the standard deviation of ΔT_A , $(1/\sqrt{3})\sigma_{\Delta T_A}$ is the standard error for the three data points, and ΔT_A is the mean of the data. The RSE varies from 0.1% to 4.6% for $R = 0.5$ – 4.5 mm at $t = 60$ s. In addition, RSE remains nearly constant for a fixed R in the range of powers studied (e.g., for $R = 0.75$ mm,

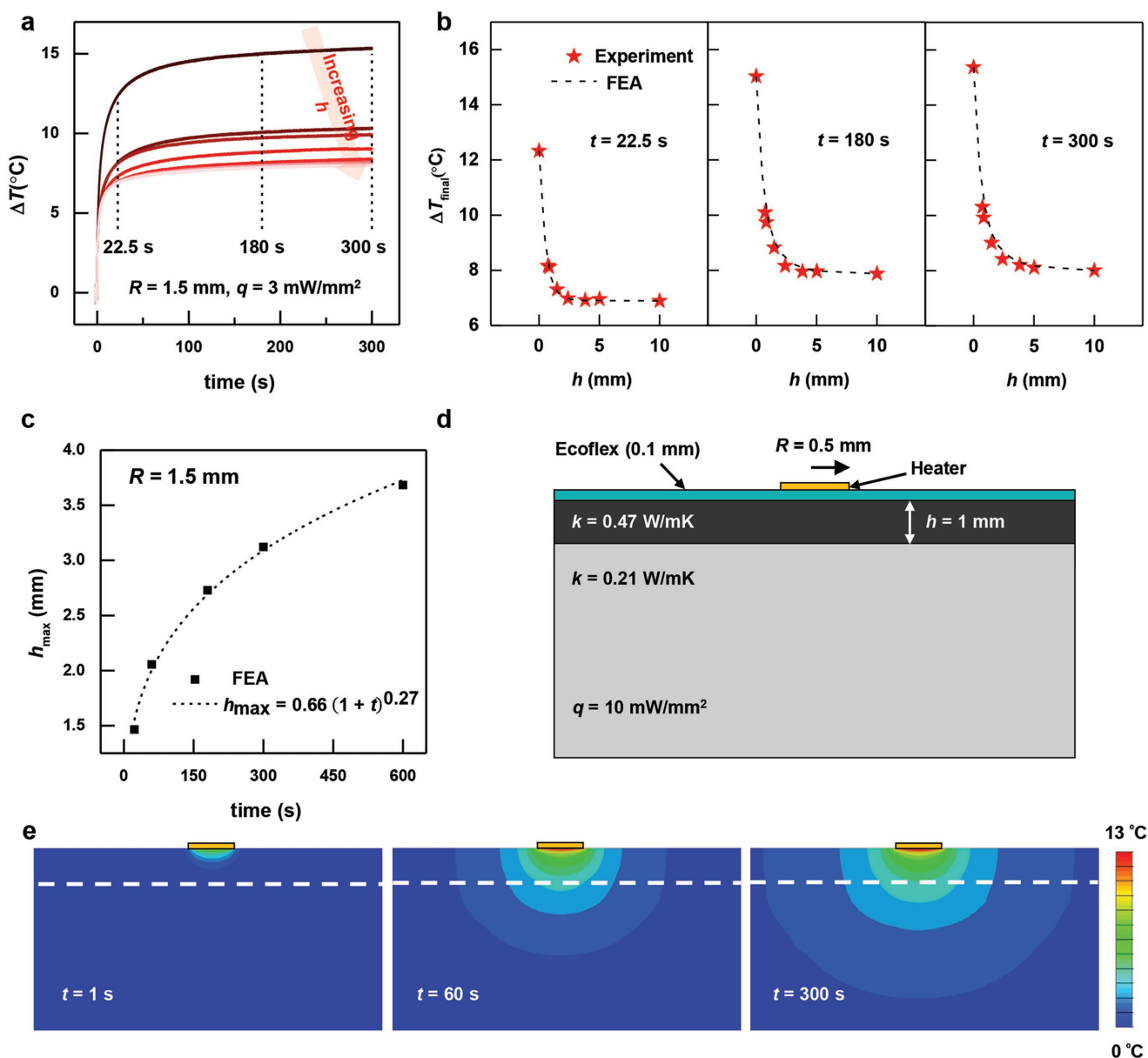


Figure 3. Dependence of the depth sensitivity on the measurement time. a) ΔT as a function of time for an e-TDS with $R = 1.5$ mm and $q = 3$ mW mm⁻². b) ΔT at $t = 22.5$, 180, and 300 s as a function of h extracted from panel (a). c) h_{\max} as a function of measurement time for an e-TDS with $R = 1.5$ mm. The dashed line represents an analytical fit of the FEA calculations with adjusted R -squared = 0.994. d) Cross-sectional schematic image showing the parameters used for FEA simulations. e) Corresponding cross-sectional temperature contour maps for $R = 0.5$ mm and $q = 10$ mW mm⁻² at measurement times of $t = 1$, 60, and 300 s.

$q = 2$ – 7 mW mm⁻², RSE = 0.22–0.23%). These findings are consistent with mean and standard deviation values that are linearly dependent on q .

Using approaches similar to those described above, h_{\max} can be determined for R between 0.5 and 4.5 mm (Figure S3, Supporting Information). The results show that h_{\max} approaches a limiting value as $R \rightarrow \infty$, which corresponds to the case where lateral heat flow is negligible and the system is approximately 1D, with heat flow predominantly into the depth of the material. Temperature contour maps derived from FEA modeling confirm this behavior (Figure 2e). Large values of R facilitate measurements of properties of deep layers of skin. The

available anatomical measurement area can, however, limit the practical size of R . In such cases, other parameters to adjust h_{\max} can be useful, as described in the following.

Additional studies reveal the dependence of h_{\max} on t , using the same bilayer silicone structure and an e-TDS with $R = 1.5$ mm and $q = 3$ mW mm⁻². Figure 3a shows the results of measurements of ΔT as a function of t with samples that have different values of h . FEA results are in good agreement with measurements, as in Figure 3b. In particular, h_{\max} increases with increasing t (Figure 3c) and eventually reaches a limiting value as $t \rightarrow \infty$ when the system achieves steady state (Figures 3d,e). Values of t should be chosen above t_{\min} to avoid

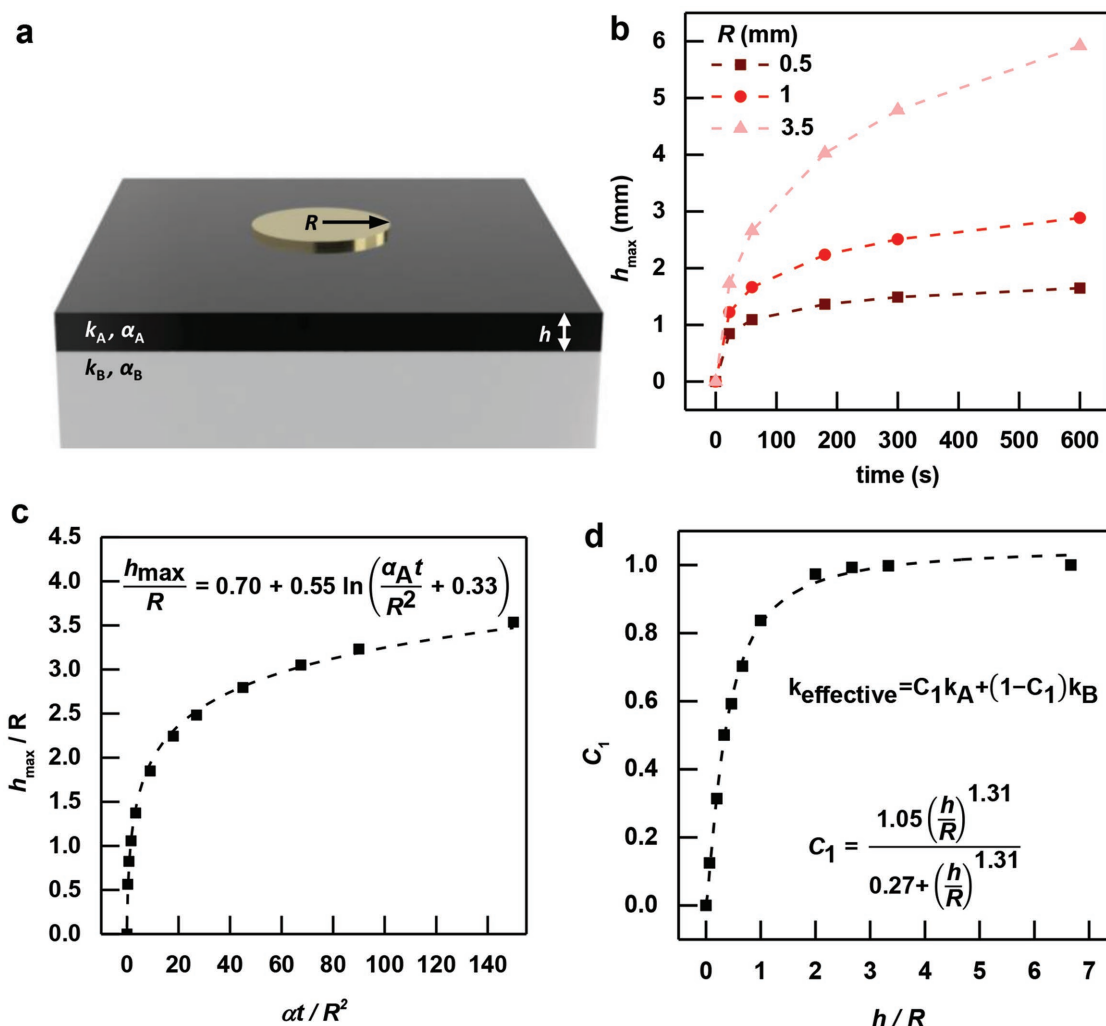


Figure 4. Summary of the essential features that define the depth sensitivity of the measurement. a) Schematic illustration of the bilayer system used for these studies. b) FEA calculations of h_{\max} as a function of t for different R and c) scaling law for critical depth as a function of R and t . The equation is a numerical fit (represented by the dotted line) with the adjusted R -squared = 0.996. d) Scaling law for constant C_1 as a function of h/R to determine $k_{\text{effective}}$. The equation is a numerical fit of the calculations (shown as a dotted line) with adjusted R -squared = 0.997.

uncertainties introduced by α . The upper bound for t based on practical considerations is in the range of a few minutes.

The dependence of h_{\max} on R and t is shown in Figure 4. FEA calculations of h_{\max} in Figure 4b indicate that the e-TDS can sense thermal properties at depths up to 6 mm. To aid in optimization of e-TDS design, an FEA-derived scaling law can be formulated that relates h_{\max} to t and R (Figure 4c). In the derivation of the scaling law (see the Supporting Information) the encapsulation layers and the substrate for the sensor are not considered explicitly, nor is the effect of air convection (Figure S4, Supporting Information). For a circular sensor placed on a bilayer system, as shown in Figure 4a, the relationship between h_{\max} , R , and t is provided in Equation (3) and Figure 4c

$$\frac{h_{\max}}{R} = g\left(\frac{\alpha_A t}{R^2}\right) \quad (3)$$

Thus, to measure the thermal properties of the top layer in a bilayer sample, the e-TDS must be designed such that $h_{\max} < h$.

Similarly, for measuring the thermal properties of the bottom layer, $h_{\max} > h$.

2.3. Extraction of an Effective Thermal Conductivity, $k_{\text{effective}}$

The aforementioned analysis mainly concerns the depth sensitivity of the measurement. In this section, the focus pertains to extraction of thermal properties for the bilayer silicone system at different depths using the measured ΔT values. Extracting k_A and k_B is difficult, due to large fitting uncertainties associated with multiple free parameters (Figure S5, Supporting Information). Instead, consider a single effective parameter, $k_{\text{effective}}$, for the bilayer system, as

$$k_{\text{effective}} = C_1 k_A + (1 - C_1) k_B \quad (4)$$

C_1 is a constant that follows the scaling law given by Equation (5) and Figure 4d

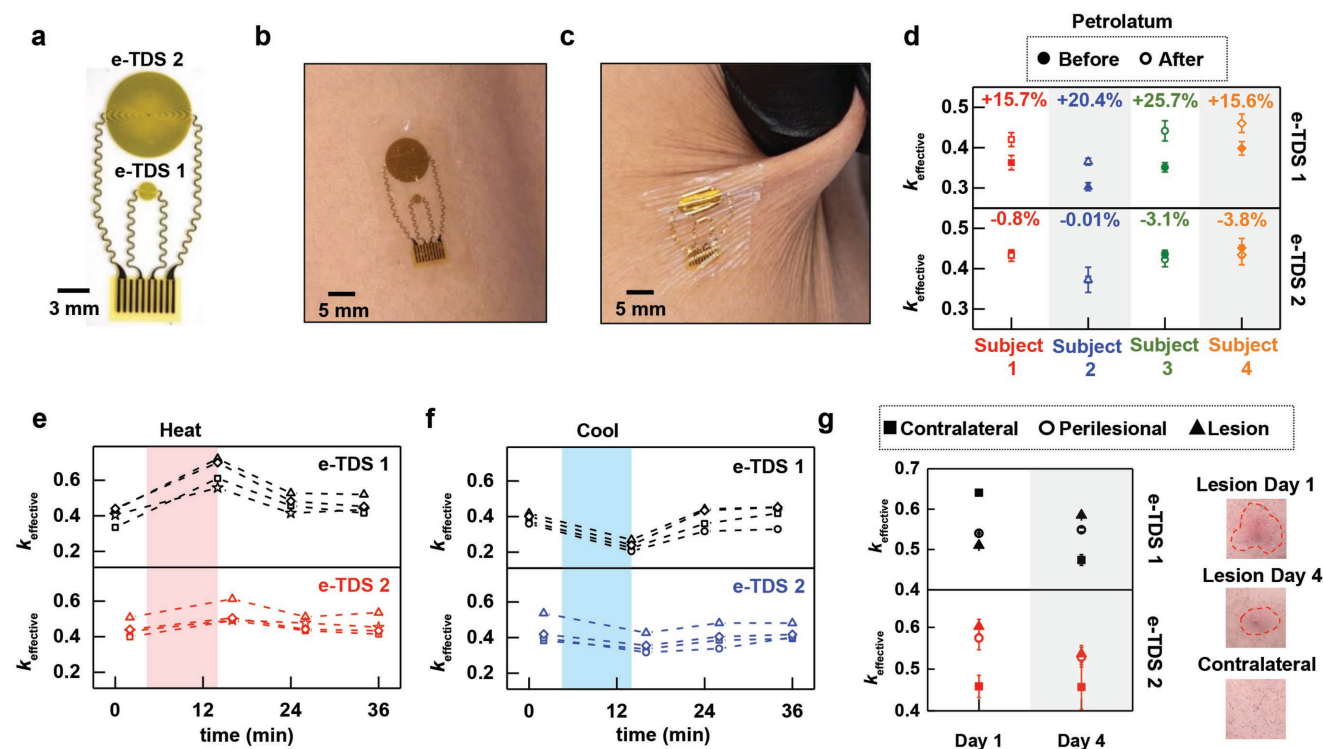


Figure 5. Experiments on human skin. a) Optical image of a dual e-TDS system with device radii $R_1 = 0.75$ mm, and $R_2 = 3.5$ mm. Image of such a system mounted on b) relaxed and c) stretched human skin demonstrating flexibility and conformity. d) Measurement of skin thermal conductivity ($k_{\text{effective}}$ (W m⁻¹ K⁻¹)) before (closed symbol) and 15 min after (open symbol) application of petrolatum for four different subjects with $q_1 = 3$ mW mm⁻² and $q_2 = 1$ mW mm⁻² for $t = 60$ s. Percentage change in $k_{\text{effective}}$ after application of petrolatum is noted above the symbols. e) $k_{\text{effective}}$ (W m⁻¹ K⁻¹) ($t = 60$ s, $q_1 = 3$ mW mm⁻² and $q_2 = 1$ mW mm⁻²) for e-TDS 1 and 2 before and 10 min after the application of heat using a hot pack on the front of the human arm for four different subjects (denoted by different symbols). The heating period is shaded in red. f) $k_{\text{effective}}$ (W m⁻¹ K⁻¹) ($t = 60$ s, $q_1 = 3$ mW mm⁻² and $q_2 = 1$ mW mm⁻²) for e-TDS 1 and 2 before and 10 min after cooling the skin on the front of the arm using a cold pack for four different subjects (denoted by different symbols). Cooling period is shaded in blue. g) Measurement of $k_{\text{effective}}$ (W m⁻¹ K⁻¹) taken 4 days apart ($t = 60$ s, $q_1 = 5$ mW mm⁻² and $q_2 = 1$ mW mm⁻²) on a cellulitis lesion, the perilesional area, and contralateral leg using the double-heater e-TDS along with corresponding images. Measurements of cellulitis were taken on one subject. The lesion on day 1 and day 4 is outlined in red.

$$C_1 = f\left(\frac{k_A}{k_B}, \frac{\alpha_A}{\alpha_B}, \frac{\alpha_A t}{R^2}, \frac{h}{R}\right) \quad (5)$$

For known values of k_A , k_B , α_A , and α_B (for $R = 1.5$ mm and $t = 60$ s), C_1 depends only on h/R (Figure 4d). From Figure 4d, for $R = 1.5$ mm, a large value of h leads to $C_1 \rightarrow 1$, and thus $k_{\text{effective}} \rightarrow k_A$ (Figure S6, Supporting Information). At large h , the spread of heat from the e-TDS is localized to the top layer, and k_A dominates the value of $k_{\text{effective}}$. For small values of h , $C_1 \rightarrow 0$ and $k_{\text{effective}} \rightarrow k_B$, consistent with a measurement depth that significantly exceeds h . Thus, for a known value of h , a sensor with small R and t such that $h_{\text{max}} < h$ enables measurement of k_A , whereas a sensor with sufficiently large R and t such that $h_{\text{max}} \gg h$ enables measurements of k_B . These observations suggest a device platform that includes a pair of e-TDS, with one configured for sensitivity to the top layer, and the other to the bottom.

2.4. Experiments on Human Skin

Using the FEA predictions in Figure 4, an ideal system of this type for studying human skin consists of e-TDS 1 with $R_1 = 0.75$ mm ($h_{\text{max}} (t = 60$ s) = 1.42 mm) and e-TDS 2 with

$R_2 = 3.5$ mm ($h_{\text{max}} (t = 60$ s) = 2.66 mm), for sensitivity to E+D and to subcutaneous fat, respectively (Figure 5a). Based on the application, or part of body under examination, values of R and t may be selected to achieve a relevant value of h_{max} . The dual e-TDS design chosen here may not be appropriate for every application, but is applicable to many locations of the body where the thickness of the E+D is ≈ 1 mm. The e-TDS is conformal and stretchable^[13] as shown in Figure 5b,c to ensure effective thermal coupling to the skin (Figure S7 in the Supporting Information describes mechanical stability). Operating the e-TDS consecutively eliminates active interference. Passive interference can be minimized by separating the peripheral edges of the two e-TDSs by an amount greater than h_{max} of e-TDS 1 (error less than 1% in ΔT). Further sources of measurement error, such as sample curvature, roughness, and local air convection, are discussed in the Supporting Information (Figures S8 and S9, Supporting Information).

A selection of on-body tests demonstrates the clinical relevance of $k_{\text{effective}}$ of human skin. For all experiments, the maximum ΔT is less than 10 °C. The values of k for healthy biological tissues are invariant to surrounding temperature, over a relevant range.^[14] The good agreement between our

simple models, which assume time-invariant constitutive properties, and the measured data suggests that active body processes do not play a significant role for the skin system being investigated. The following experiments use healthy, normal skin of the same subject as a reference for quantifying changes in thermal properties. This reference point, for introduced changes, corresponds to the same location just before the relevant changes are introduced, and for other cases, the contralateral location on the body. Thus, changes in thermal properties are measured on an individual basis, eliminating the need for absolute comparisons to a single reference point. Three consecutive measurements yield error bars to account for effects of air convection and human motion. In some cases, the error bars are too small to be visualized beyond the symbols (i.e., <1%).

The first studies examine the effect of petrolatum (Vaseline and Unilever), an occlusive moisturizer.^[15] Measurements involve four subjects evaluated before, and 15 min after the application of $\approx 5 \text{ mg cm}^{-2}$ of petrolatum to the forearm. In all cases, $k_{\text{effective}}$ extracted from e-TDS 1 increases by 15–25%, while the value extracted from e-TDS 2 remains nearly unchanged. These results suggest modulation of the properties only of superficial tissue, the stratum corneum ($\approx 100 \mu\text{m}$). The finding that $k_{\text{petrolatum}} = 0.19 \text{ W m}^{-1} \text{ K}^{-1}$ (determined using e-TDS 1, see Figure S10, Supporting Information) indicates that the e-TDS does not measure a change due to the thermal properties of petrolatum, but rather to an increase in $k_{\text{effective}}$ by prevention of transepidermal water loss (TEWL), consistent with previous studies using conventional devices for measuring TEWL.^[15c]

Measurements that involve localized skin heating and cooling (Figure 5e,f) illustrate the ability to determine $k_{\text{effective}}$ at intermediate depths ($\approx 500 \mu\text{m}$ to 1 mm). The former involves application of a hot pack (average temperature = 46–48 °C, HotHands Super Warmers) to the front of the arm for 10 min. Recording $k_{\text{effective}}$ before, immediately after, and at two consecutive 10 min intervals after the heating period captures the responses of the skin to the applied heat. The $k_{\text{effective}}$ determined from e-TDS 1 increases dramatically after heating, consistent with increased blood flow. e-TDS 2 also measures a significant rise in $k_{\text{effective}}$, but to a lesser extent than e-TDS 1, thereby suggesting the depth of tissue affected by the hot pack is larger than that affected by petrolatum. Over time, $k_{\text{effective}}$ approaches its initial value. Localized cooling induces dermal changes due to constriction of blood flow. After 10 min of cooling, the front of the arm with a cold pack (average temperature = 9–11 °C, Instant Cold Pack, Primacare), measurements of $k_{\text{effective}}$ from e-TDS 2 indicate changes smaller than those from e-TDS 1 for all four patients. The results suggest that the effects of localized cooling occur mainly in the dermis, similar to the case for heating.

One clinical application for this technology is as a diagnostic aid for cellulitis. Cellulitis is a potentially fatal infection of the deep dermis and subcutaneous tissue, with 14 million cases annually resulting in more than 600,000 yearly hospital admissions.^[4a] However, 30–40% of cellulitis cases are misdiagnosed given similar clinical presentations of common mimicking conditions that do not require antibiotics (e.g., venous stasis dermatitis).^[4a] Currently, there is

no existing laboratory or imaging tool approved for the diagnosis of this common condition. Studies reported here suggest the ability of the e-TDS system to detect changes in the deep dermis and subcutaneous fat (Figure 5g) in one case of cellulitis. Measurements with e-TDS 1 and 2 applied to the center of a cellulitis lesion, its perilesional area, and the corresponding location on the healthy, contralateral leg (as an internal control) allow the study of cellulitis on a single patient. Values of $k_{\text{effective}}$ determined with e-TDS 1 show no apparent temporal changes in the thermal conductivity at the lesion or perilesional area (k_{lesion} and $k_{\text{perilesional}}$). By contrast, e-TDS 2 shows evidence of inflammation, since $k_{\text{contralateral}} < k_{\text{perilesional}} < k_{\text{lesion}}$. $k_{\text{contralateral}}$ on day 1 and day 4 remains constant for e-TDS 2, but not for e-TDS 1. The thermal properties of the superficial E+D vary greatly on a scale of days due to ambient conditions and hydration state, so this disagreement between $k_{\text{contralateral}}$ for day 1 and day 4 for e-TDS 1 is not unexpected. The deep dermis and fat, however, do not display variations in thermal properties to this extent because they are insulated from ambient changes by the epidermis. On day 4 of measurement, k_{lesion} and $k_{\text{perilesional}}$ approach $k_{\text{contralateral}}$, suggesting healing, which is also apparent from the optical image on day 4. These results indicate a clear decrease in erythema and lesion size in contrast to the image taken on day 1 (the lesion diameter decreases from $\approx 2.5 \text{ cm}$ to $\approx 1 \text{ cm}$). The ability to measure thermal properties of tissue at different depths may improve diagnostic discrimination of conditions such as cellulitis (minimal superficial or epidermal change but significant deep dermal subcutaneous fat change) with mimickers such as venous stasis dermatitis (greater epidermal inflammation). Depth profiling human skin is thus essential to the clinical applications of e-TDS, as different skin conditions have different thermal characteristics.

3. Conclusion

The findings reported here suggest that e-TDS technology enables monitoring of thermal properties of human tissue at depths of up to $\approx 6 \text{ mm}$. Detailed studies of the thermal physics associated with the measurement quantify the key design parameters that define the depth sensitivity, thereby allowing controlled, and targeted measurements for various skin conditions. Capabilities of the e-TDS system include detection of subtle changes in skin hydration, microvascular blood flow, and composition as a function of tissue depth. Depth sensitivity to subcutaneous fat may create new opportunities for diagnostics across a wide range of cutaneous and systemic diseases, and the noninvasive, reusable nature of the devices promotes at-home use for long-term monitoring.^[2c,4a] The e-TDS platform may offer a valuable alternative to invasive diagnostic approaches and costly imaging techniques.

Opportunities for future work include the development of a wireless system for control and data extraction and expanded clinical studies on patients with various diseases to further define the diagnostic relevance of thermal depth sensors. In certain unique anatomical locations, the epidermis, dermis, and

subcutaneous fat have a total thickness of <6 mm, thereby enabling interrogation of tissues beneath the skin. Such locations include the eyelid (<2 mm in thickness) or areas overlying bony prominences (e.g., trochanter, sacrum, or ischium, <4 mm in thickness).^[16] Thus, these sensors could be useful in assessing the joint space or bone for signs of infection (osteomyelitis) or bleeding (hemoarthrosis).

4. Experimental Section

FEA to Determine Critical Depth: The commercial software ABAQUS was used to study the thermal response of the e-TDS device on the surface of single-layer or bilayer samples. Here, the e-TDS was a resistive sensor encapsulated by a layer of PI (1.6 μm thickness; $k_{\text{PI}} = 0.52 \text{ W m}^{-1} \text{ K}^{-1}$ and $\alpha_{\text{PI}} = 0.32 \text{ mm}^2 \text{ s}^{-1}$ ^[6b,11]) on both sides and printed on a layer of Ecoflex (100 μm thickness; $k_{\text{Ecoflex}} = 0.21 \text{ W m}^{-1} \text{ K}^{-1}$ and $\alpha_{\text{Ecoflex}} = 0.11 \text{ mm}^2 \text{ s}^{-1}$ ^[6b]) that contacted the sample, as illustrated in Figure 1a. Figure S2a (Supporting Information) and Figure 4a show FEA models of the e-TDS (the resistive sensor was approximated as a circle with the same outer contour and total power) placed on single-layer and bilayer samples, respectively. The air convection coefficient was $6 \text{ W m}^{-2} \text{ K}^{-1}$ as determined from Figure S8 (Supporting Information). The following two FEA models were compared to study the depth sensitivity: (1) the bilayer sample (top layer: silicone A, thickness h , $k_{\text{A}} = 0.47 \text{ W m}^{-1} \text{ K}^{-1}$ determined by measurement of the pure, single-layer sample, and $\alpha_{\text{A}} = 0.14 \text{ mm}^2 \text{ s}^{-1}$ found from literature;^[17] bottom layer: silicone B, $k_{\text{B}} = 0.21 \text{ W m}^{-1} \text{ K}^{-1}$ determined by measurement of the pure, single-layer sample, $\alpha_{\text{B}} = 0.11 \text{ mm}^2 \text{ s}^{-1}$ found from literature^[6b]) as in Figure 4a; and (2) the single-layer sample (pure silicone A) as shown in Figure S2a (Supporting Information). The definitions of the sensitivity and critical thickness (h_{max}) for FEA are the same as those for the scaling law. Figure S11a,b shows the sensitivity as a function of h for different R and t . Figure 4c shows that h_{max} and thus sensitivity increase with R and t .

Fabrication of Epidermal Thermal Depth Sensors: Spin-coating (3000 rpm) a thin ($\approx 200 \text{ nm}$) layer of poly(methyl methacrylate) (PMMA A4, MicroChem) onto a carrier substrate (e.g., silicon wafer, glass slide, or glass wafer) followed by baking at $180 \text{ }^\circ\text{C}$ for 3 min formed a sacrificial release layer. Next, spin-coating a film of poly(amic) acid (PI-2545, HD Microsystems) onto the same substrate at 5000 rpm, followed by baking on a hot plate at $90 \text{ }^\circ\text{C}$ for 30 s, then at $150 \text{ }^\circ\text{C}$ for 5 min, and finally at $250 \text{ }^\circ\text{C}$ for 1 h in a vacuum oven yielded a $\approx 1.6 \text{ }\mu\text{m}$ thick layer of PI as electrical insulation. Electron beam evaporation formed a bilayer of Ti (20 nm) and Au (100 nm). Photolithography and wet etching defined metal traces for the devices.

Spin-coating and curing poly(amic) acid using the conditions mentioned above formed an upper insulation layer. These two layers of PI placed the metal in the neutral-mechanical plane, thereby minimizing strains due to bending/stretching. Photolithography and reactive ion etching (O_2 plasma, March RIE) patterned the PI in geometries that match those of the metal traces. Immersion in acetone dissolved the PMMA sacrificial layer, to allow removal of the structures from the carrier substrate onto the surface of a piece of water-soluble tape (Water-Soluble Wave Solder Tape, 3M). Sputter deposition of $\approx 70 \text{ nm}$ of SiO_2 onto the reverse side of the structure created a reactive surface for chemical bonding. Separately, spin-coating (1000 rpm, 100 μm) a low modulus formulation of silicone (Ecoflex, Smooth-On) onto a glass slide coated with a thin layer of PMMA produced a thin, soft elastomer support. Exposure to UV light functionalizes the surface of the silicone with $-\text{OH}$ groups for bonding to the SiO_2 -coated surface of the sensor structure. Immersion in boiling water dissolved the water-soluble tape. Drying the sensors by baking in an oven at $70 \text{ }^\circ\text{C}$ and pressure bonding using a hot iron set to $193 \text{ }^\circ\text{C}$ of thin cables (ACF, Elform) as connections to a current source completed the fabrication process.

Transient Plane Source Measurements: The TPS measurements used a commercial constant current source (Keithley 6220) to set the thermal power per unit area, q . The resultant heating led to changes in resistance, Δr , determined by corresponding changes in voltage, ΔV , recorded with a digital multimeter (National Instruments). The measured Δr allowed determination of ΔT through the temperature coefficient of resistance (TCR) of Au. Each sensor was carefully calibrated against measurements using an infrared (IR) camera to determine the TCR (Figure S1, Supporting Information). After applying heating current for the measurement time, application of low current for the same time cooled the sensor down such that $\Delta T = 0 \text{ }^\circ\text{C}$. Typical applied currents for the q used in this study were $<1.5 \text{ mA}$. However, because of the PI electrical insulation layer, and Ecoflex substrate, no current enters the skin.

Heat Transport Studied with Thermochromic Pigment/Ecoflex: A single sensor ($R = 1.5 \text{ mm}$) laminated onto a substrate of Ecoflex mixed with thermochromic pigment (Temperature Activated Thermochromic Bi-Color Powder Pigment, Atlanta Chemical Engineering) defined the experimental layout in Figure 1c–e and the parameters for the FEA temperature maps assume the thermal conductivity $k_{\text{silicone}} = 0.21 \text{ W m}^{-1} \text{ K}^{-1}$ and $\alpha_{\text{silicone}} = 0.11 \text{ mm}^2 \text{ s}^{-1}$ ^[6b] respectively. This thermochromic pigment changed the color from black to pink at or above $25 \text{ }^\circ\text{C}$. The experiments involved observations in an ambient laboratory environment ($T = 22 \text{ }^\circ\text{C}$) and $q = 10 \text{ mW mm}^{-2}$.

Fabrication of Bilayer PDMS Structures: Mixing the base and curing agent at a ratio suggested by the vendor (10:1; Sylgard 184, Dow Corning) followed by curing at room temperature for $\approx 24 \text{ h}$ yielded the silicone B elastomer. All experiments used the same 15 mm thick cylindrical sample of silicone B with diameter $d = 100 \text{ mm}$ to maintain a constant sample temperature approximation. The conditions for constant sample temperature were thickness $> 2\sqrt{\alpha t}$ and $d > 2(2\sqrt{\alpha t} + R)$, which were maintained. Synthesis of silicone A (Sylgard 170, Dow Corning) involved a separate mixing step for the individual base and curing agent for 3–5 min, followed by combining the two components together at a ratio of 1:1 for an additional 3 min. The specific gravity of silicone A provided by the vendor multiplied by the volume of a cylindrical sample ($d = 100 \text{ mm}$) of height h determines the masses of mixture required to create different h of silicone A, producing the measurement samples. The thicknesses of these samples ranged from 0.5 to 10 mm in steps of 1.0–5 mm. Curing occurred at room temperature for $\approx 24 \text{ h}$. Measurements with digital calipers with 0.01 mm resolution yielded the thicknesses of these silicone A samples. Physically laminating a film of this type onto the silicone B substrate formed the bilayer silicone A/silicone B structures for testing. The reversible van der Waals adhesion allowed repetitive lamination and removal of such films to yield a collection of samples with only a single silicone B substrate. A shallow plastic dish covered the devices during measurements to minimize effects of air convection.

On-Body Experiments: Each subject gave full informed consent before participating in on-body experiments. Nine different subjects participated across the four unique on-body tests. For all tests, chosen values of q (and thus applied current, I) ensured that $\Delta T_{t=60 \text{ s}} < 10 \text{ }^\circ\text{C}$. The first test served to demonstrate detection of superficial (epidermal, $\approx 100 \text{ }\mu\text{m}$) changes using the e-TDS system. Four healthy/normal subjects (female, age 23; male, Age 22; female, age 27; and male, age 23) participated in this experiment. Subjects sat still in a laboratory setting during the test. A commercial occlusive moisturizer, petrolatum (Vaseline and Unilever) served to induce changes in hydration level in the stratum corneum and epidermis. Placing the dual e-TDS system first on each subject's bare forearm allowed measurement of thermal properties. First, e-TDS 1 measured ΔT as a function of t for a duration of 60 s, followed by a 60 s cooling period when the sensor was OFF, allowing the sensor to return to its initial temperature. Then, e-TDS 2 measured ΔT as a function of t for the same duration (60 s), followed by a cooling period of the same time (60 s). Repeating measurements by e-TDS 1 and e-TDS 2 three times each produced the data, with symbols as the mean of the data and error bars representing the standard

deviations. The e-TDS system was peeled off the forearm (pen marks on the forearm denoted the location of the dual e-TDS system). Applying 5 mg cm⁻² of petrolatum to each subject's volar forearm and waiting for 15 min allowed for a sufficient increase in hydration. Laminating the dual e-TDS system on the subjects' volar forearm according to the corresponding marked locations and repeating the measurements for both e-TDS 1 and e-TDS 2, three times each, completed the experiment. In Figure 5d, the symbols represent the mean of the data for each individual subject, and the error bars represent the corresponding standard deviations.

The next test involved changes in blood flow due to application of commercial heating and cooling packs to induce changes in blood flow at intermediate depths (dermis, 100 μm to 1 mm). Four healthy/normal subjects (female, age 26; male, age 22; female, age 23; and male, age 18) were participated in the heating pack study for blood vessel dilation and four other healthy/normal subjects (male, age 30; female, age 23; female, age 21, and male, age 18) participated in the cooling pack study for blood vessel constriction. Subjects sat relatively still in a laboratory environment during the tests. The procedure for heating/cooling pack studies was identical, as described here. The dual e-TDS was applied to the front of each subjects' arm. Pen marks identified the location of the device on the skin. In the same way for the first on-body experiment, e-TDS 1 measured ΔT as a function of t for a duration of 60 s, followed by a 60 s cooling period when the sensor was OFF, allowing the sensor to return to its initial temperature. Then, e-TDS 2 measured ΔT as a function of t for the same duration (60 s), followed by a cooling period of the same time (60 s). The sensors were removed from the arm. The commercial heating or cooling pack was placed on the location marked by pen for 10 min. Removing the heating or cooling pack and laminating the sensors back onto the skin according to the marked location prepared the subject for subsequent measurements. Measurements taken immediately, 10 min, and 20 min after removal of the hot/cold pack from the skin completed the study. In this case, measurements were only taken one time for each time interval (for both e-TDS 1 and 2) because the effects of the hot/cold pack were transient, as the data in Figure 5e,f show evidence that the skin returns to normal over time, as expected. However, because four randomly chosen subjects showed similar trends for both tests, the results were consistent.

The final test involved measurements on a cellulitis lesion. Only one subject participated in the study since cellulitis is not an induced change, in contrast to the studies mentioned above. The subject (male, age 30) had cellulitis on his left leg (thigh). The subject removed hair from the area of the cellulitis lesion using a pair of tweezers to ensure conformal contact between the device and skin. Measurements taken on 1 day, and 4 days following comprised the study. Measuring ΔT as a function of t on the two separate days with e-TDS 1 and e-TDS 2 sequentially, three times each, on the center of the cellulitis lesion, perilesional area, and contralateral leg produced the data in Figure 5g. Images of the contralateral leg, and the cellulitis lesion taken on the two separate days, also appear in Figure 5g.

Supporting Information

Supporting Information is available from the Wiley Online Library or from the author.

Acknowledgements

S.R.M. and Y.M. contributed equally to this work. The authors would like to thank Prof. Kaitlyn Crawford for useful discussions. This work was supported by the Center for Bio-Integrated Electronics in the Simpson/Querrey Institute at Northwestern University. Y.M. and X.F. acknowledge support from the National Basic Research Program of China (Grant No. 2015CB351900) and the National Natural Science Foundation

of China (Grant Nos. 11402135 and 11320101001). Y.H. acknowledges support from NSF (Grant Nos. 1400169, 1534120, and 1635443). The studies utilized the Northwestern University Micro/Nano Fabrication Facility (NUFAB), which is partially supported by Soft and Hybrid Nanotechnology Experimental (SHyNE) Resource (NSF ECCS-1542205), the Materials Research Science and Engineering Center (DMR-1720139), the State of Illinois, and Northwestern University.

Conflict of Interest

The authors declare no conflict of interest.

Keywords

depth sensing, epidermal electronics, monitoring skin health, thermal conductivity, thermal sensors

Received: March 23, 2018

Revised: May 9, 2018

Published online: June 25, 2018

- [1] J. Kottner, A. Lichterfeld, U. Blume-Peytavi, *Br. J. Dermatol.* **2013**, *169*, 528.
- [2] a) M. N. Sawka, S. J. Montain, W. A. Latzka, *Comp. Biochem. Physiol., Part A: Mol. Integr. Physiol.* **2001**, *128*, 679; b) L. S. Jutte, M. A. Merrick, C. D. Ingersoll, J. E. Edwards, *Arch. Phys. Med. Rehabil.* **2001**, *82*, 845; c) P. V. Pople, K. K. Singh, *Int. J. Pharm.* **2012**, *434*, 70.
- [3] a) P. Clarys, R. Clijsen, J. Taeymans, A. O. Barel, *Skin Res. Technol.* **2012**, *18*, 316; b) E. Alanen, J. Nuutinen, K. Nicklen, T. Lahtinen, J. Monkkonen, *Skin Res. Technol.* **2004**, *10*, 32; c) J. E. Tooke, J. Ostergren, B. Fagrell, *Int. J. Microcirc.: Clin. Exp.* **1983**, *2*, 277; d) M. Vogt, H. Ermert, *IEEE Trans. Ultrason., Ferroelectr., Freq. Control* **2005**, *52*, 375; e) F. Mirrashed, J. C. Sharp, *Skin Res. Technol.* **2004**, *10*, 149; f) J. Welzel, C. Reinhardt, E. Lankenau, C. Winter, H. H. Wolff, *Br. J. Dermatol.* **2004**, *150*, 220.
- [4] a) A. B. Raff, D. Kroshinsky, *JAMA, J. Am. Med. Assoc.* **2016**, *316*, 325; b) Q. Weng, A. B. Raff, J. M. Cohen, N. Gunasekera, J.-P. Okhovat, P. Vedak, C. Joyce, D. Kroshinsky, A. Mostaghimi, *JAMA Dermatol.* **2017**, *153*, 141.
- [5] a) T. Someya, Y. Kato, T. Sekitani, S. Iba, Y. Noguchi, Y. Murase, H. Kawaguchi, T. Sakurai, *Proc. Natl. Acad. Sci. USA* **2005**, *102*, 12321; b) R. C. Webb, A. P. Bonifas, A. Behnaz, Y. Zhang, K. J. Yu, H. Cheng, M. Shi, Z. Bian, Z. Liu, Y. S. Kim, W. H. Yeo, J. S. Park, J. Song, Y. Li, Y. Huang, A. M. Gorbach, J. A. Rogers, *Nat. Mater.* **2013**, *12*, 938.
- [6] a) R. C. Webb, Y. Ma, S. Krishnan, Y. Li, S. Yoon, X. Guo, X. Feng, Y. Shi, M. Seidel, N. H. Cho, J. Kurniawan, J. Ahad, N. Sheth, J. Kim, J. G. t. Taylor, T. Darlington, K. Chang, W. Huang, J. Ayers, A. Gruebele, R. M. Pielak, M. J. Slepian, Y. Huang, A. M. Gorbach, J. A. Rogers, *Sci. Adv.* **2015**, *1*, e1500701; b) L. Tian, Y. Li, R. C. Webb, S. Krishnan, Z. Bian, J. Song, X. Ning, K. Crawford, J. Kurniawan, A. Bonifas, J. Ma, Y. Liu, X. Xie, J. Chen, Y. Liu, Z. Shi, T. Wu, R. Ning, D. Li, S. Sinha, D. G. Cahill, Y. Huang, J. A. Rogers, *Adv. Funct. Mater.* **2017**, *27*, 1701282; c) S. Krishnan, Y. Shi, R. C. Webb, Y. Ma, P. Bastien, K. E. Crawford, A. Wang, X. Feng, M. Manco, J. Kurniawan, E. Tir, Y. Huang, G. Balooch, R. M. Pielak, J. A. Rogers, *Microsyst. Nanoeng.* **2017**, *3*, 17014; d) R. C. Webb, R. M. Pielak, P. Bastien, J. Ayers, J. Niittynen, J. Kurniawan, M. Manco, A. Lin, N. H. Cho, V. Malychuk, G. Balooch, J. A. Rogers, *PLoS One* **2015**, *10*, e0118131.

- [7] S. E. Gustafsson, *Rev. Sci. Instrum.* **1991**, *62*, 797.
- [8] a) A. Koh, S. R. Gutbrod, J. D. Meyers, C. Lu, R. C. Webb, G. Shin, Y. Li, S. K. Kang, Y. Huang, I. R. Efimov, J. A. Rogers, *Adv. Healthcare Mater.* **2016**, *5*, 373; b) Y. Hattori, L. Falgout, W. Lee, S. Y. Jung, E. Poon, J. W. Lee, I. Na, A. Geisler, D. Sadhwani, Y. Zhang, Y. Su, X. Wang, Z. Liu, J. Xia, H. Cheng, R. C. Webb, A. P. Bonifas, P. Won, J. W. Jeong, K. I. Jang, Y. M. Song, B. Nardone, M. Nodzenski, J. A. Fan, Y. Huang, D. P. West, A. S. Paller, M. Alam, W. H. Yeo, J. A. Rogers, *Adv. Healthcare Mater.* **2014**, *3*, 1597; c) L. Gao, Y. Zhang, V. Malyarchuk, L. Jia, K. I. Jang, R. C. Webb, H. Fu, Y. Shi, G. Zhou, L. Shi, D. Shah, X. Huang, B. Xu, C. Yu, Y. Huang, J. A. Rogers, *Nat. Commun.* **2014**, *5*, 4938.
- [9] K. R. Holmes, Thermal Properties, <http://users.ece.utexas.edu/~valvano/research/Thermal.pdf> (accessed: May 2017).
- [10] a) Y. Lee, K. Hwang, *Surg. Radiol. Anat.* **2002**, *24*, 183; b) O. Akkus, A. Oguz, M. Uzunlulu, M. Kizilgul, *J. Diabetes Metab.* **2012**, *3*, 216.
- [11] Dupont, Dupont Kapton Summary of Properties, <http://www.dupont.com/kapton/general/H-38479-4.pdf> (accessed: February 2017).
- [12] M. L. Cohen, *J. Invest. Dermatol.* **1977**, *69*, 333.
- [13] S. Wang, M. Li, J. Wu, D.-H. Kim, N. Lu, Y. Su, Z. Kang, Y. Huang, J. A. Rogers, *J. Appl. Mech.* **2012**, *79*, 031022.
- [14] J. W. Valvano, J. R. Cochran, K. R. Diller, *Int. J. Thermophys.* **1985**, *6*, 301.
- [15] a) R. Ghadially, L. Halkier-Sorensen, P. M. Elias, *J. Am. Acad. Dermatol.* **1992**, *26*, 387; b) A. V. Rawlings, D. A. Canestrari, B. Dobkowski, *Dermatol. Ther.* **2004**, *17*, 49; c) R. L. Rietschel, *J. Invest. Dermatol.* **1978**, *70*, 152.
- [16] a) K. Hwang, D. J. Kim, S. H. Hwang, *J. Craniofacial Surg.* **2006**, *17*, 54; b) E. Yalcin, M. Akyuz, B. Onder, H. Unalan, I. Degirmenci, *J. Spinal Cord Med.* **2013**, *36*, 225.
- [17] Professional Plastics, Thermal Properties of Plastic Materials, <https://www.professionalplastics.com/professionalplastics/ThermalPropertiesofPlasticMaterials.pdf> (accessed: February 2017).